Combined mesoscale/experimental study of selective placement of magnetic nanoparticles in diblock copolymer films via solvent vapour annealing

P. Posocco,[a,b] Y. Mohamed Hassan,[a,c] I. Barandiaran,[d] G. Kortaberria,[d] S. Pricl[a,b,*] and M. Fermeglia[a]

We present a combined theoretical/experimental study to investigate the effect of selective solvent vapor annealing treatment on the obtainement of highly ordered morphologies of symmetric poly(styrene-*b*-methyl methacrylate) diblock copolymer (PS-*b*-PMMA DBC) films loaded with compatibilized magnetic (Fe_3O_4) nanoparticles (NPs). Different amounts of NPs were considered (1, 2, and 5% wt) to study the effect of the inorganic content on the final properties of Fe_3O_4/PS-*b*-PMMA films. A precise control of the DBC nanostructure could be obtained by very simple and cost-effective fabrication steps, compatible with current industrial processes. Moreover, the modified NPs could be selectively placed into the PMMA domains of the DBC up to NP concentration of 5% wt while preserving the corresponding DBC lamellar morphology.

[a] *Molecular Simulation Engineering Laboratory (MOSE), Department of Engineering and Architecture (DEA), University of Trieste, 34127 Trieste, Italy*
[b] *National Interuniversity Consortium for Material Science and Technology (INSTM), Research Unit MOSE-DEA, University of Trieste, 34127 Trieste, Italy*
[c] *Technical University of Denmark, Department of Micro- and Nanotechnology, Ørsteds Plads, DK - 2800 Kgs. Lyngby, Denmark (present address)*
[d] *Materials + Tecnhologies Group, Euskal Herriko Unibertsitatea (UPV/EHU), Plaza de Europa 1, 20018 Donostia, Spain*

Introduction

The self-assembly of diblock copolymer (DBC) films has become increasingly important as a method for nanoscale patterning, and there has been a growing interest in the study of thin heterogeneous films, both theoretically[1,2] and experimentally.[3,4] DBCs offer a bottom-up approach to nanoscale fabrication with feature sizes of the order of nanometers. From a technological standpoint, the self-assembly of DBCs provides a simple method for making a variety of 2D periodic or complex patterns, resulting from the controlled aggregation/organization of the two incompatible polymeric blocks into cylindrical, spherical, or lamellar domains.

It is well understood that the equilibrium morphology, periodicity, interfacial width, and diffusivity of each DBC system depend on the Flory-Huggins interaction parameter (χ), the degree of polymerization (N), and the volume fraction of each block (f).[5] Moreover, microphase separation and/or significant reordering or morphology changes of DBC microdomains can be achieved employing various experimental approaches.[6-9] One of these consists in solvent vapour annealing (SVA) treatment at ambient temperature. SVA enables tuning the periodicity and the morphology over a wide range,[10] and has the advantage of reversibility, with microdomains morphology changes upon solvent vapour conditions modifications.[11]

On the other hand, magnetic nanoparticles (NPs) have received special attention due to its potential applications in many diverse fields such as ferrofluids, magnetic resonance imagining, biomedicine and drug delivery.[12-14] Engineering the self-assembly of those NPs within block copolymer nanodomains is useful in the design of periodic structures to form materials with enhanced mechanical strength as well as to achieve unique optical, electronic and magnetic properties at the nanometer scale, for applications in solar cells, catalysts or high density magnetic storage media.[15-17] To overcome the problem of the tendency of NPs to aggregate due to their high surface area and surface energy, and to facilitate their dispersion in a selected block of a DBC, surface functionalization aimed at increasing their compatibility with the matrix has been one of the most adopted and successful routes.[18]

However, the use of neat DBCs for modified-NPs dispersion still presents some disadvantages as, for instance, very low equilibration, which may result in the systems being kinetically trapped in a long-lived metastable state.[19] Solvent based processing of DBCs has the potential to overcome these difficulties. A selective solvent can swell polymer chains and increase the relative volume of the DBC domain where nanoparticles are preferentially located. Therefore, exploring the possibility of using nanostructures formed by solvated DBCs for NPs dispersion is of great merit.

Under this perspective, in this paper we present a combined simulated/experimental study to investigate the effect of selective SVA treatment on the obtainment of highly ordered morphologies of symmetric poly(styrene-b-methyl methacrylate) block copolymer (PS-b-PMMA) films. Film structures were predicted by mesoscale simulations and then compared with the relative experimental systems. In addition, simulations were further employed to examine how different amounts (1, 2, and 5 wt %) of surface-modified Fe3O4 NPs affect the final properties of the relevant DBC/NP films. To the purpose, 3-methacryloxypropyltrimethoxysilane (MPTS) was the NP compatibilizer of choice, in order to promote selective NPs location within the PMMA block of the DBC. All relevant nanocomposite morphologies were next experimentally probed by AFM analysis.

Materials and methods

Materials

Magnetite (Fe_3O_4) nanoparticles (nominal size 9 nm) were purchased from Integram Technologies, Inc. MPTS with 98 % of purity, was purchased from ABCR. PS-*b*-PMMA block

copolymer (f_{PS} = f_{PMMA} = 0.5) was purchased from Polymer Source, Inc.. The number average molecular weight of both PS and PMMA blocks is 80.000 g/mol, with a polydispersity of 1.09.

Nanoparticle modification

Fe_3O_4 NPs were first modified with MPTS.[20] Scheme 1 shows the reaction scheme of the silanization process. This reaction implies a nucleophilic attack of the NP –OH surface groups to the Si atoms of MPTS. 0.05 g of nanoparticles and 10 µmol of silane were mixed by sonication into 40 mL of toluene. The reaction was carried out under inert atmosphere for 3 hours at 60 ºC. The resulting MPTS-functionalized NPs were subsequently washed with THF and dried in vacuum for 72 h at 40 ºC.

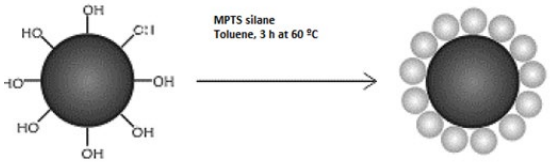

Scheme 1. Reaction scheme of the silanization process

FTIR and TGA measurements (see Supplementary Information for details and Figures S1 and S2), were used to assess the successful modification of the NPs with the organic compound, and to determine the amount of grafted compatibilizer.[21] The surface density of the silane was about 3.1 molecules/nm^2. A direct comparison of the surface density of hydroxyl groups (8.1 molecules/nm^2) with that of the silane on the NP surface yielded a reaction efficiency of 38.3 %.

DBC and nanocomposite preparation

Nanocomposites were prepared by mixing PS-*b*-PMMA block copolymer with the silanized Fe_3O_4 NPs. Accordingly, the NPs were dispersed in toluene for two hours by sonication, followed by PS-*b*-PMMA block copolymer addition. Thin films of both neat block copolymer and nanocomposite were then prepared by spin-coating onto Si(100) wafers at 2000 rpm for 120 s using a Telstar Instrumat P-6708D spin-coater. The film thickness, as measured by AFM after sample scratching, was around 100 nm for all investigated samples. For selective solvent annealing, thin films were exposed to saturated acetone vapors (selective for PMMA, with χ_{PMMA} = 0.18 and χ_{PS} = 1.1)[22] at increasing times in a closed vessel and kept at room temperature following spin-coating without removing the residual solvent. After vapor exposure, samples were removed and stored at ambient atmosphere before characterization. For nanocomposite films, the appropriate exposure time was chosen in order to obtain a lamellar morphology for the neat DBC. Nanocomposites were prepared at three different NP content: 1, 2, and 5 wt%, respectively.

Characterization techniques

Surface morphologies obtained for different films were studied by atomic force microscopy with a scanning probe microscopy AFM Dimension ICON of Bruker, operating in tapping mode (TM–AFM). An integrated silicon tip/cantilever, from the same manufacturer, having a resonance frequency of around 300 kHz, was used. Measurements were performed at a scan rate of 1 Hz/s, with 512 scan lines.

DPD theory

Dissipative Particle Dynamics (DPD)[23,24] simulations are an effective tool for modelling structural phenomena like self-assembly of diblock copolymers in melt and in solution,[25,26] polymer nanocomposites,[27,28,29] and membranes[30] under various solvent conditions, just to mention a few.

In a DPD simulation,[24] the actual material (solvents, nanoparticles or polymer chains) is modeled as a collection of spherical particles or beads that represent lumps of the material. DPD particles are defined by mass m_i, position $\boldsymbol{r}_i$, and velocity $\boldsymbol{v}_i$, and interact with each other via a total force $\boldsymbol{F}$ that is the sum of a conservative force $\boldsymbol{F}^C$, dissipative force $\boldsymbol{F}^D$, and a random force $\boldsymbol{F}^R$:

$$\boldsymbol{F} = \boldsymbol{F}^C + \boldsymbol{F}^D + \boldsymbol{F}^R \tag{1}$$

$\boldsymbol{F}^C$ typically includes non-bonded interaction between beads i and j:

$$\boldsymbol{F}^C = \begin{cases} a_{ij}(1 - r_{ij}/r_c)\boldsymbol{r}_{ij} & (r_{ij} \le r_c) \\ 0 & (r_{ij} \ge r_c) \end{cases} \tag{2}$$

where a_{ij} and $\boldsymbol{r}_{ij} = \boldsymbol{r}_i - \boldsymbol{r}_j$ are the maximum repulsion and the separation vector between particles i and j, respectively, while r_c is the cut-off distance at which the influence of $\boldsymbol{F}^C$ vanishes.

The remaining two forces, $\boldsymbol{F}^D$ and $\boldsymbol{F}^R$, which arise from degrees of freedom neglected by coarse-graining, are given by:

$$\boldsymbol{F}^D = -\gamma_{ij}\omega^D(r_{ij})\left(\frac{\boldsymbol{r}_{ij}}{r_{ij}} \cdot \boldsymbol{v}_{ij}\right)\frac{\boldsymbol{r}_{ij}}{r_{ij}} \tag{3}$$

$$\boldsymbol{F}^R = \sigma_{ij}\omega^R(r_{ij})\frac{\zeta_{ij}}{\sqrt{\Delta t}}\frac{\boldsymbol{r}_{ij}}{r_{ij}} \tag{4}$$

where $\omega^D(r_{ij})$ and $\omega^R(r_{ij})$ are weight functions that vanish for $r_{ij} \ge r_c$, γ_{ij} is the friction coefficient, σ_{ij} is the noise amplitude, $\boldsymbol{v}_i = \boldsymbol{v}_i - \boldsymbol{v}_i$ is the velocity vector, $\zeta_{ij} = \zeta_{ji}$ is a Gaussian random number with zero mean and unit variance that is chosen independently for each pair of interacting particles, and Δt is the time step. The pair-wise dissipative and random forces guarantee that momentum is locally conserved and this, in turn, ensures correct hydrodynamic behavior.

Espanol and Warren[31] showed that a DPD system samples the canonical ensemble and obeys the fluctuation-dissipation theorem if the following relationships hold:

$$\omega^D(r_{ij}) = \left[\omega^R(r_{ij})\right]^2 \tag{5}$$

$$\sigma_{ij}^2 = 2\gamma_{ij}k_BT \tag{6}$$

where k_BT is the Boltzmann constant and T the equilibrium temperature. $\omega^D(r_{ij})$ and $\omega^R(r_{ij})$ are typically chosen as[23]:

$$\omega^D(r_{ij}) = \left[\omega^R(r_{ij})\right]^2 = \left(1 - \frac{r_{ij}}{r_c}\right)^2 \qquad (r_{ij} < r_c)$$
$$= 0 \qquad (r_{ij} \geq r_c) \tag{7}$$

Finally, when modeling chains, another force is active in the system, i.e., a harmonic spring connecting two adjacent particles i and j:

$$\boldsymbol{F}^S = K_b(r_{ij} - r_0)\frac{\boldsymbol{r}_{ij}}{r_{ij}} \tag{8}$$

where K_b is the spring stiffness and r_0 is the equilibrium distance between the particles.

Mesoscale models

In our pursuit to properly mimic the DBC self-assembly and SVA process, we simulated self-organization via solvent evaporation and solvent annealing at the mesoscale level. The effect of solvent evaporation was reproduced in the DPD framework according to the procedure proposed by Neratova et al.[32] Briefly, the DBC solution (3% wt of polymer in toluene) was placed on an impenetrable, fixed, substrate.[33] Next, an exchange phase and a gas phase, respectively, were created on top of the film phase. During the DPD simulations, when solvent particles left the film phase and appeared in the exchange region, they were transformed into gas particles. As a result of such process, the fraction of the gas phase increased, while the thickness of the film decreased. Gas and polymer phases were assumed to be immiscible.

Once each equilibrium film thickness was reached, the film was subjected to a virtual SVA process, inspired by the approach proposed by Potemkin et al.[34]. Briefly, the gas phase was "cut out" from the simulation box and the space above the film was filled-in by a homogenous mixture of particles modeling air and solvent (i.e., acetone) molecules. Again, air was completely immiscible with the DBC film and solvent molecules were able to penetrate inside PS and PMMA domains but with different affinity. The volume fraction of the solvent molecules can be considered as a measure of partial pressure. Thus, a proper solvent concentration was chosen to reproduced acetone vapor pressure p^* at room temperature (p^* = 139.6 mmHg[35]).

The same computational procedure was applied to simulate the dispersion of Fe_3O_4 nanoparticles in the films, starting from a homogenous mixture of toluene, PS-*b*-PMMA, and magnetite.

At DPD level the types of particles present in the system were the following: solvent particles (denoted by St and Sa to distinguish between toluene and acetone), gas particles (G), PS- and PMMA-beads forming the DBC chain (S and M), substrate (W), and Fe_3O_4 nanoparticles (F). Since we focused on lamellar forming DBCs, we fixed the total length of the chain N to 40 with a relative fraction of each block equal to 0.5.

Chemical interactions between particles were expressed by the conservative force $\boldsymbol{F}^C$ via the interaction parameter a_{ij}, which in general could be estimated from the Flory-Huggins interaction parameter according to the formula[36] $\chi_{ij} = (0.286 \pm 0.002)(a_{ij}-a_{ii})$ at $\rho = 3$. For DBC particles (i.e. S and M beads), we applied the relationship proposed by Glotzer et al.[37]

$$a_{ij} = a_{ii} + 3.27\left(1 + \frac{3.9}{N^{0.51}}\right)\chi_{ij} \tag{9}$$

N is the total length of the flexible chain and a_{ij} are expressed in terms of r_c/k_BT units, where k_B is the Boltzmann constant, T the equilibrium temperature, and r_c is the cut-off radius.

χ_{ij} in Eq. (9) is defined in terms of the solubility parameters of the i and j components as:

$$\chi_{ij} = \frac{V_{DPD}}{k_B T}(\delta_i - \delta_j)^2 \tag{10}$$

where V_{DPD} is the volume of DPD bead and δ_i is the solubility parameters of the i-th component, which is in turn related to the cohesive energy density e_{coh}.[38]

Further, solvent and air were considered as a homogenous mixture ($a_{i/G}$ = 25, where i refers to St and Sa beads)[34], and air was supposed to be immiscible with the remaining components ($a_{i/G}$ = 50; $a_{PS/G}$ was set to 45 due to the slightly lower surface energy of PS with respect to PMMA[39]).

Due to the high grafting density (3.1 chains/nm^2), NPs were assumed to be fully covered by MPTS molecules, thereby screening out gold-gold interactions; thus, the solubility parameter of MPTS was calculated according to the group contribution approach.[40]

The complete set of DPD parameters is reported in Table 1.

In all DPD studies the following reduced units were used: r_c (unit of length), m (mass of a DPD particle), and k_BT (unit of energy). Simulations were carried out in a box of 67 x 67 x 60 with a time step of Δt = 0.03 and simulation periods of at least 5 x 10^5 steps or longer were adopted until stable morphology was observed. Periodic boundary conditions were imposed in lateral directions.

Table 1 DPD interaction parameters

a_{ij}	G	St	Sa	S	M	W	F
G	25.0						
St	25.0	25.0					
Sa	25.0	50.5	25.0				
S	45.0	26.6	28.8	25.0			
M	50.0	26.2	25.6	31.7	25.0		
W	50.0	30.0	30.0	25.0	25.0	25.0	
F	50.0	25.2	25.8	34.9	26.2	30.0	25.0

Results and discussion

Effect of solvent vapour annealing on PS-*b*-PMMA diblock microphase separation

As pointed out by several authors,[41] ordered microphase morphologies in PS-*b*-PMMA DBC systems can be obtained by exposing the corresponding films to solvent vapor selective for PMMA (e.g., acetone). After solvent exposure, since PMMA is more soluble in acetone than PS, a strong attraction between polymer and solvent is realized when they get in contact, leading to polymer swelling. Concomitantly, the net interaction between polymer segments becomes repulsive. Diffusion of solvent to the DBC film surface plays an important role in obtained morphology. Taking all this into account, several microphase-separated morphologies have been observed by different authors

for PS-*b*-PMMA depending on exposure time and film thickness: hexagonally packed nanocylinders, lamellar, or striped morphologies.[22, 41, 42,43,44,45]

Accordingly, in this work the development of microstructure in approximately 100 nm thick PS-*b*-PMMA copolymer films upon different exposure times to acetone vapours was followed in parallel by mesoscale simulations and imaging techniques. Acetone was chosen as selective solvent for PMMA, after consideration of the solubility parameters of each block and solvent.[22]

Figure 1 shows the morphology predicted for the PS-*b*-PMMA film without SVA treatment at ambient temperature. As it is clear from the picture, the film exhibits microphase separation yet with no clear pattern. This can be easily explained by considering that, during the preparation process, a sufficient amount of solvent is present in the film to promote microdomains formation. However, the solvent is quickly evaporated before the DBC equilibrium state can be achieved, essentially freezing the morphology in a metastable or disordered state.

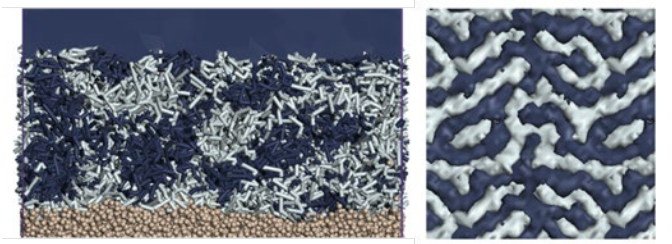

Figure 1. Lateral (left) and top (right) view of PS-b-PMMA film morphology as obtained from mesoscale simulations in the absence of SVA treatment. Grey: PMMA regions, dark blue: PS regions. The substrate is depicted as light brown spheres.

The disordered character of this structure was also confirmed by the analysis of the orientation order parameter. The time-resolved orientation order parameter S is measured by the Saupe tensor:[46]

$$Q_{\mu\nu} = \frac{3}{2}\left(\boldsymbol{r}_\mu \boldsymbol{r}_\nu - \frac{1}{3}\delta_{\mu\nu}\right) \qquad (11)$$

where $\boldsymbol{r}$ is a unit vector directing along the bond, which connects the PS-block and the PMMA-block in a single diblock chain, μ and ν are Cartesian indices, and δ is the Knocker symbol. The largest eigenvalue of the volume average of $Q_{\mu\nu}$ (denoted as S) is the orientation order parameter. According to its definition, then, the achievement of a high-value, persistent plateau in the time course of S might be taken as an evidence of structural equilibration of the system under investigation.

From Figure 2 we see that the SVA-untreated PS-*b*-PMMA DBC system indeed undergoes reorganization from the initial completely random disorder morphology; however, the final value of S around 0.005 confirms that the system does not microsegregate into a specific ordered structure.

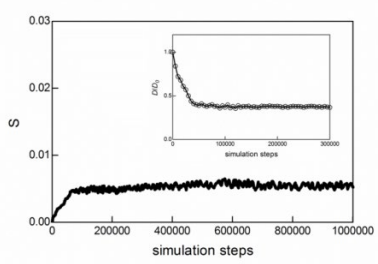

Figure 2. Time evolution of the orientation order parameter S during toluene evaporation as calculated from DPD simulation. In the inset the film thickness contraction D/D_0 is highlighted.

Next, for characterizing the SVA-untreated film properties, we analysed the degree of drying, defined as the ratio between the film thickness D at a given time t and the initial film thickness D_0 (Figure 2). As expected from the order parameter behaviour, the film initially contracts due to the solvent evaporation and then reaches a minimum value of D/D_0 around 0.38 when the structure stabilizes.

The surface morphology of the PS-*b*-PMMA film mimicked by simulation was experimentally assessed by AFM, as shown in Figure 3: the presence of indistinct bright/dark domains confirm the lack of orientational alignment of the underlying DBC structure.

Figure 3. AFM phase image of SVA-untreated PS-*b*-PMMA film after spin coating. Lighter regions: PMMA domains; darker regions: PS domains.

Next, we went on analysing the effect of acetone vapour treatment on PS-*b*-PMMA films morphology after spin coating. From the time-evolution of the orientation order parameter S reported in Figure 4 a clear reorganization of the copolymer morphology as a result of the exposure to the solvent can be observed. At the same time, the change in block organization is paralleled by a different degree of film swelling until saturation occurs. This is due to the fact that solvent diffusion is a morphology-controlled process, as evidenced in previous studies.[34]

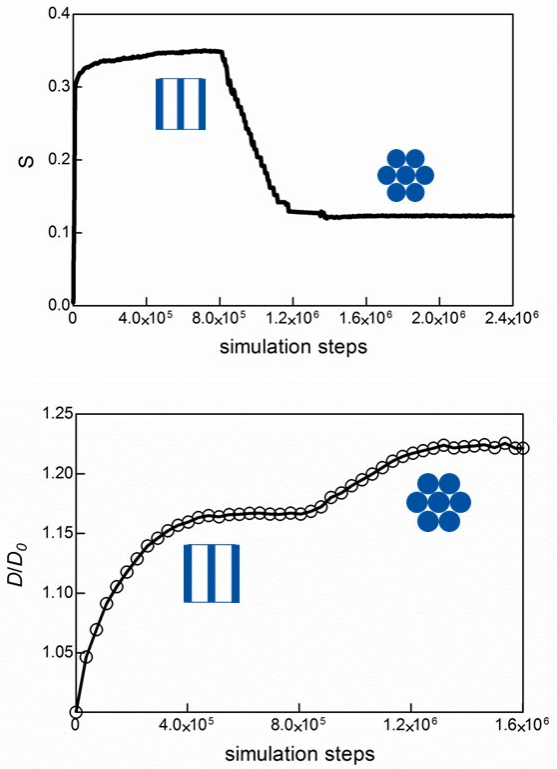

Figure 4. Time evolution of the orientation order parameter S (top) and film swelling D/D_0 (bottom) during virtual SVA of the PS-*b*-PMMA DBC film with acetone at ambient temperature.

Figure 5 reports the film morphology as obtained from mesoscale simulation after approximately $7x10^5$ simulation steps. It is clear that a surface-perpendicular lamellar microphase morphology was obtained, with typical well-ordered PMMA and PS domains of repeat-spacing of 81 nm.

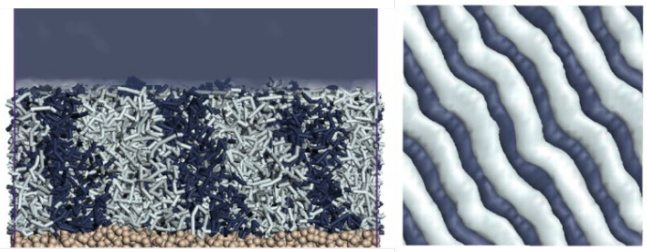

Figure 5. Lateral (left) and top (right) view of PS-*b*-PMMA film morphology as obtained from mesoscale simulation after approximately $7x10^5$ steps of exposure to acetone vapours. Grey: PMMA regions, dark blue: PS regions. The substrate is depicted as light brown spheres.

When the vapour exposure was prolonged (i.e., calculation time extended), the relevant simulation showed a morphology consisting on PS hexagonally packed cylinders oriented perpendicularly to the free surface, characterized by a diameter of 48 nm and a center-to-center distance of 54 nm, as reported in Figure 6.

Aside from visual inspection and orientation order parameter calculation, the organization of the PS and PMMA domains was further assessed through the calculation of the structure factor $S(q)$. The structure factor $S(q)$ was derived from simulation using the following relationship:[47]

$$(\boldsymbol{q}) = \frac{(\sum_j \cos(\boldsymbol{q}\cdot\boldsymbol{r}_j))^2+(\sum_j \sin(\boldsymbol{q}\cdot\boldsymbol{r}_j))^2}{N} \quad (12)$$

where $\boldsymbol{q}$ is the wave vector and $\boldsymbol{r}_j$ is the position of jth particle of type PS or PMMA.

As shown in Figure 7, the calculated structure factor $S(q)$ values confirm[48] that the film morphology corresponds to a lamellar (after approximately $7x10^5$ simulation steps) and cylindrical (after approximately $2x10^6$ simulation steps) organization.

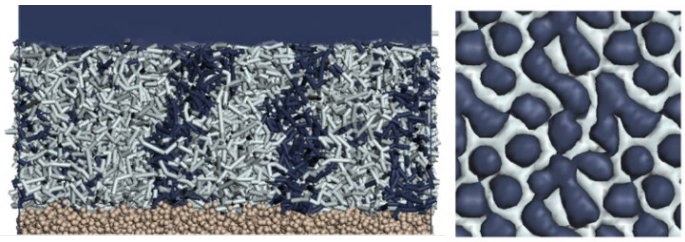

Figure 6. Lateral (left) and top (right) view of PS-b-PMMA film morphology as obtained from mesoscale simulation after prolonged ($2x10^6$ steps) of exposure to acetone vapours. Grey: PMMA regions, dark blue: PS regions. The substrate is depicted as light brown spheres.

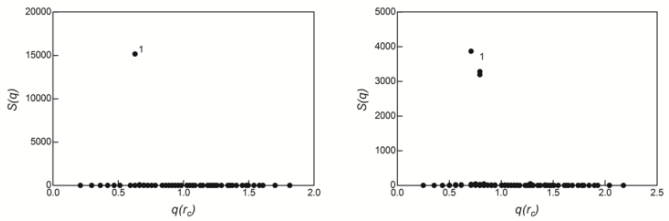

Figure 7. Structure factor $S(q)$ calculated from simulation of PS block in the lamellar (after approximately $7x10^5$ simulation steps) (left) and cylindrical (after approximately $2x10^6$ simulation steps) (right) morphology.

Pleasingly, the simulated morphologies were nicely confirmed by the AFM images of the corresponding surfaces, as shown in Figures 8 and 9, where brighter regions correspond to the PMMA block, since PMMA has a modulus higher than PS at room temperature.[22,49] After 16h of SVA treatment, a surface-perpendicular lamellar microphase morphology is detected, with an average inter-lamellar distance of 77 nm. PMMA and PS lamellae are 68 and 8 nm wide, respectively. This morphology is the prototypical equilibrium state phase structure in symmetric diblock copolymer films.[22] Of note, simulations and AFM indicated that, despite the equivalent fraction of the two blocks, the domains are characterized by a large asymmetry in their relevant dimensions, the lamellae of PMMA being much larger than those of PS. This dimensional asymmetry can be easily justified by considering that, since acetone is a selective solvent for PMMA, its molecules tend to remain within the methacrylate domains. Hence, the PMMA blocks have more chance to relax and assume a stretched configuration, while the PS blocks tend to aggregate to minimize the contacts with the solvent and the free energy of the film. As a result, the PMMA chains form thicker domains, (or the matrix phase of the film in the case of longer exposure time), while the PS blocks form thin lamellae (or cylinders when the annealing time is extended).

Lastly, AFM characterization reveals that 26h of treatment leads to an in-plane cylindrical hexagonal order of the PS domains, thereby confirming the microphase segregation morphology evolution predicted by mesoscale simulations. The measured center-to-center distance between cylinders is of 49.2 nm.

In aggregate, the above results allows to conclude that solvent exposure time plays a key role in the controlling the structural evolution of the PS-*b*-PMMA DBC film microphase separation.

Selective placement of Fe_3O_4 nanoparticles into PS-*b*-PMMA lamellae

Mastering dispersion and selective location of nanoparticles in ordered block copolymer nanostructures can pave the way for the design and production of engineered nanomaterials with enhanced mechanical, electrical, or magnetic properties. In this spirit, the ultimate goal of the present effort was indeed the achievement of a proper and specific dispersion of MPTS-modified Fe_3O_4 NPs within PMMA lamellae of a PS-*b*-PMMA DBC.

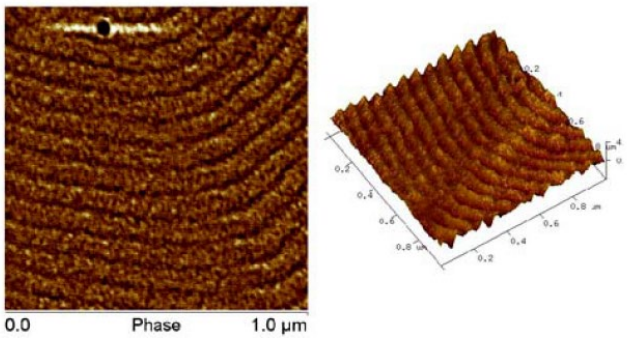

Figure 8. AFM phase image (left) and 3D height (right) of PS-*b*-PMMA film after exposure to SVA treatment with acetone for 16h. Lighter region: PMMA domains; darker regions: PS domains.

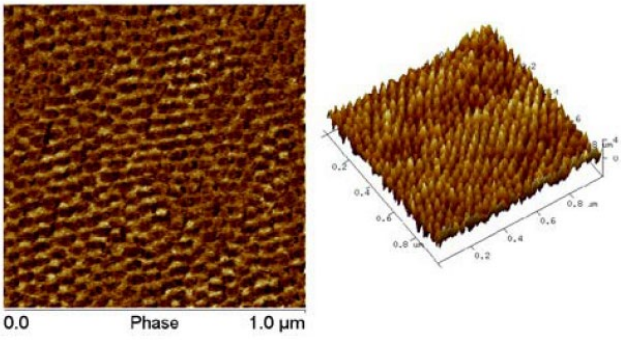

Figure 9. AFM phase image (left) and 3D height (right) of PS-*b*-PMMA film after exposure to SVA treatment with acetone for 26h. Lighter regions: PMMA domains; darker regions: PS domains.

Therefore, on the basis of the foregoing discussion, a SVA exposure time of 16h was selected to ensure the obtainment of PS-*b*-PMMA DBC nanometric films characterized by lamellar morphologies, and the effects MPTS-modified Fe_3O_4 NPs addition on the relevant nanocomposites was investigated at three different NP concentrations: 1, 2, and 5 wt %.

The DPD simulated equilibrium morphologies of DBC/NP films at increasing NP loading are shown in Figure 10, while the corresponding surfaces obtained by AFM are shown in Figure 11 for comparison.

Both simulation and AFM characterization reveal that NPs addition do not prevent the self-assembly of the PS-*b*-PMMA DBC matrix, and do not induce further lateral microphase segregation, the lamellar morphology being maintained independently of the content of the inorganic part. Moreover, simulations predicted that, at all concentrations considered, the NPs could be selectively dispersed via SVA into the PMMA phase, as assessed by the corresponding bead density profiles calculated along a direction perpendicular to the lamellar orientation at equilibrium (Figure 11, bottom panels). The simulations further reveal that, at 1 wt% loading, the NPs are preferentially located in the middle of the PMMA domains; increasing concentration (2 and 5 wt%) does not result in a change of selectivity but only in a higher spatial occupation of the PMMA lamellae. At the same time solvent molecules are selectively adsorbed into the PMMA domains, with concentration decreasing as NP concentration rises. with concentration decreasing as NP concentration rises.

The eventual degree of NP aggregation, in term of size and shape of NP clusters, was characterized through the cluster gyration tensor R_g^2 and shape asphericity A_s, respectively.[50] The mean square radius of gyration is defined as:

$$\langle R_g^2 \rangle = \langle \frac{1}{N} \sum_i \left(r_i - r_{i,cm} \right)^2 \rangle \quad (13)$$

where r_i are the components of the position coordinates (x,y,z) of the center of mass of a NP and $r_{i,cm}$ are the components of the position coordinates of the CM of a cluster (x_{cm}, y_{cm}, and z_{cm}). N is the number of NPs present in a cluster. The eigenvalues of the matrix are R_1^2, R_2^2, and R_3^2. The asphericity A_s of a cluster can be defined as follows:[51]

$$A_s = \frac{\sum_{i>j=1}^{3} \left(\langle R_i^2 \rangle - \langle R_j^2 \rangle \right)^2}{2 \left(\sum_{i=1}^{3} \langle R_i^2 \rangle \right)^2} \quad (14)$$

Accordingly, A_s is equal to 0 for a perfect sphere and 0.5 for a cylinder. Cluster gyration tensor R_g^2 and asphericity A_s analysis from simulation reveals that only limited aggregation of the NPs occurs in all cases, the most concentrated nanocomposite (5 wt%) showing the largest (albeit still quite modest) degree of NP aggregation. The system loaded with NPs at 1 wt% is characterized by the presence of small, almost spherical NP clusters (A_s = 0.03), with average size R_g of 42 nm. Increasing NP concentration (2 wt%) results in more elongated NPs clusters (A_s = 0.36), with average size of 69 nm.

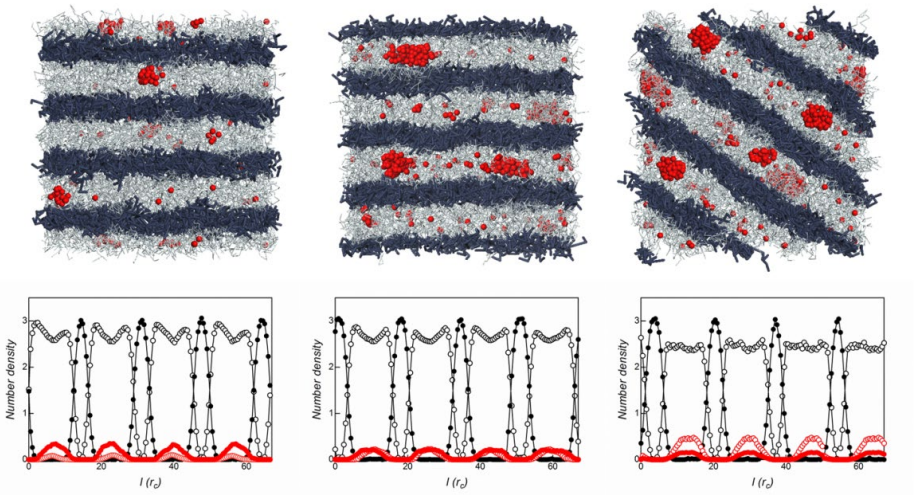

Figure 10. (Top) Mesoscale morphology (top view) of PS-*b*-PMMA striped thin film filled with 1%, 2%, and 5% wt MTPS-modified Fe_3O_4 NPs (from left to right). PS chains are represented as blue sticks, PMMA with grey sticks, while NPs as shown as red spheres. (Bottom) One-dimensional bead density profiles for the systems in the top panel. Diagram legend: black points, PS; white points, PMMA; empty red points, NP; filled red points, solvent.

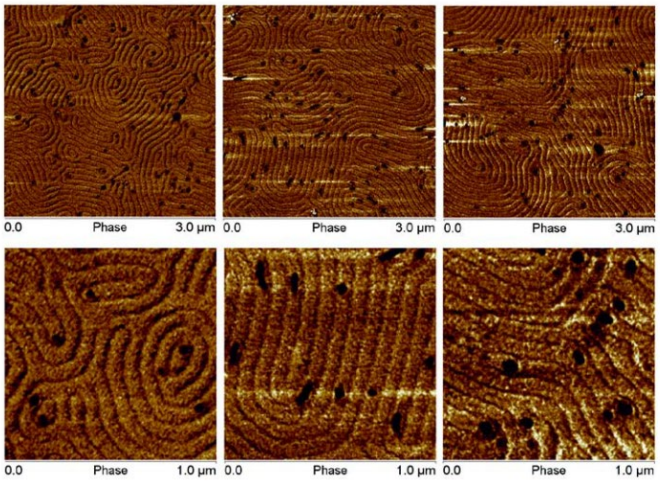

Figure 11. AFM phase images at different magnifications (top 3 x 3 µm; bottom 1 x 1 µm) for PS-*b*-PMMA films filled with 1 (left), 2 (center) and 5 wt% (right) of MTPS-modified Fe_3O_4 nanoparticles after exposition to acetone vapours for 16h. The lighter regions are PMMA domains, the darker zones correspond to PS domains.

Finally, at the highest NP concentration (5 wt%), nearly spherical clusters are again observed (A_s = 0.08), with average diameters around 76 nm, always located in the PMMA phase.

AFM inspections of the corresponding experimental systems fully confirm computer predictions. Thus, the right panels of Figure 11 show small clusters of almost spherical shape and diameter of 38 nm, essentially dispersed in the PMMA phase for 1 wt% NP concentration. When the NP content is increased to 2% wt (middle panels in Figure 11), the aggregates become elongated. Typical length is in the range of 80-100 nm, with an average height of 38 nm. At the highest concentration considered (right panels in Figure 11), NPs are present in form of nearly spherical agglomerates of 68 nm, still mainly located in the PMMA domains. Therefore, although NPs cluster formation are predicted and experimentally verified at all NPs concentrations, their dimensions correspond to the aggregation of few NPs, being the nominal diameter of a single equal to 9 nm (see Materials and methods). Accordingly, we can conclude that the modification of Fe_3O_4 via MPTS decoration and the use of SVA methodology allowed to satisfactorily and selectively disperse magnetite NPs into the PMMA lamellar region of the corresponding PS-*b*-PMMA DBC, at least up to a concentration of 5 wt% NPs.

Conclusions

Polymer-based nanocomposites have gained popularity in the last two decades due to their exciting bulk and surface properties. However, the current bottleneck for the exploitation of the theoretical excellent properties of these systems is the complete dispersion of the nanoparticles in the matrix and the consequent development of a large interfacial area. Complete NP dispersion will allow maximizing the available matrix–particle interphase, thereby optimizing the organic–inorganic interaction responsible of the enhanced properties of the final material.

So, most of the research efforts in this area have been focused on developing rational processing strategies for polymer nanocomposites and in promoting better matrix–particle interactions.

In this scenario, through combined mesoscale simulations and experimental study we investigated the development of highly ordered morphologies in symmetric poly(styrene-b-methyl methacrylate) block copolymer films loaded with MPTS modified magnetic nanoparticles and subjected to selective solvent vapor annealing treatment (SVA).

Calculations and experiments showed that the presence of PMMM-selective solvent (i.e., acetone) induced controlled microphase separation of PS and PMMA blocks in lamellar morphology for shorter exposure times (16 h) or in in-plane PS cylindrical hexagonal pattern for longer exposure times (26 h). Lamellar morphology was preserved after the addition of nanoparticles at all concentrations considered. A satisfactory and selective dispersion of MPTS-modified Fe_3O_4 nanoparticles into the PMMA lamellar-region of SVA annealed PS-b-PMMA film was achieved up to a concentration of 5 wt % Although nanoparticle cluster formation were predicted and experimentally verified at all NPs concentrations, their average dimensions correspond to the aggregation of few NP units.

Acknowledgments

Financial support from the Basque Country Government (Grupos Consolidados, IT776-13) and the Ministry of Education and Innovation (MAT2015-66149-P) is gratefully acknowledged.

References

1. S.-M. Hur, G. S. Khaira, A. Ramírez-Hernández, M. Müller, P. F. Nealey and J. J. de Pablo, *ACS Macro Letters*, 2015, **4**, 11-15.
2. A. F. Hannon, W. Bai, A. Alexander-Katz and C. A. Ross, *Soft Matter*, 2015, **11**, 3794-3805.
3. T.-W. Kim, H. Choi, S.-H. Oh, G. Wang, D.-Y. Kim, H. Hwang and T. Lee, *Adv. Mater.*, 2009, **21**, 2497-2500.
4. J. W. Jeong, W. I. Park, L.-M. Do, J.-H. Park, T.-H. Kim, G. Chae and Y. S. Jung, *Adv. Mater.*, 2012, **24**, 3526-3531.
5. N. P. Balsara, *Curr. Opin. Solid State Mater. Sci.*, 1999, **4**, 553-558.
6. H. Jung, S. Woo, Y. Choe, D. Y. Ryu, J. Huh and J. Bang, *ACS Macro Letters*, 2015, **4**, 656-660.
7. C. C. Kathrein, W. Bai, J. A. Currivan-Incorvia, G. Liontos, K. Ntetsikas, A. Avgeropoulos, A. Böker, L. Tsarkova and C. A. Ross, *Chem. Mater.*, 2015, **27**, 6890-6898.
8. A. Modi, S. M. Bhaway, B. D. Vogt, J. F. Douglas, A. Al-Enizi, A. Elzatahry, A. Sharma and A. Karim, *ACS Applied Materials & Interfaces*, 2015, **7**, 21639-21645.
9. L.-Y. Shi, H. Li, W.-W. Lei, W. Ni, R. Ran, Y. Pan, X.-H. Fan and Z. Shen, *Nanoscale*, 2015, **7**, 17756-17763.
10. A. Baruth, M. Seo, C. H. Lin, K. Walster, A. Shankar, M. A. Hillmyer and C. Leighton, *ACS Applied Materials & Interfaces*, 2014, **6**, 13770-13781.
11. W.-H. Huang, P.-Y. Chen and S.-H. Tung, *Macromolecules*, 2012, **45**, 1562-1569.
12. A. Kondo and H. Fukuda, *Colloids Surf. Physicochem. Eng. Aspects*, 1999, **153**, 435-438.
13. H.-b. Shen, D.-h. Long, L.-z. Zhu, X.-y. Li, Y.-m. Dong, N.-q. Jia, H.-q. Zhou, X. Xin and Y. Sun, *Biophys. Chem.*, 2006, **122**, 1-4.
14. I. Garcia, N. E. Zafeiropoulos, A. Janke, A. Tercjak, A. Eceiza, M. Stamm and I. Mondragon, *J. Polym. Sci., Part A: Polym. Chem.*, 2007, **45**, 925-932.
15. M. R. Bockstaller, R. A. Mickiewicz and E. L. Thomas, *Adv. Mater.*, 2005, **17**, 1331-1349.
16. S. Park, D. H. Lee, J. Xu, B. Kim, S. W. Hong, U. Jeong, T. Xu and T. P. Russell, *Science*, 2009, **323**, 1030-1033.
17. C. Goh, K. M. Coakley and M. D. McGehee, *Nano Lett.*, 2005, **5**, 1545-1549.
18. I. Barandiaran and G. Kortaberria, *RSC Advances*, 2015, **5**, 95840-95846.
19. V. Ganesan, *J. Polym. Sci., Part B: Polym. Phys.*, 2008, **46**, 2666-2671.
20. I. Barandiaran and G. Kortaberria, *Eur. Polym. J.*, 2015, **68**, 57-67.
21. C. Cosio-Castañeda, R. Martínez-García and L. M. Socolovsky, *Solid State Sci.*, 2014, **30**, 17-20.
22. Y. Xuan, J. Peng, L. Cui, H. Wang, B. Li and Y. Han, *Macromolecules*, 2004, **37**, 7301-7307.
23. R. D. Groot and P. B. Warren, *J. Chem. Phys.*, 1997, **107**, 4423-4435.
24. P. J. Hoogerbrugge and J. M. V. A. Koelman, *Europhys. Lett.*, 1992, **19**, 155-160.
25. S. Ma, D. Qi, M. Xiao and R. Wang, *Soft Matter*, 2014, **10**, 9090-9097.
26. P. Posocco, M. Fermeglia and S. Pricl, *J. Mater. Chem.*, 2010, **20**, 7742-7753.
27. J.-H. Huang and X.-Z. Li, *Soft Matter*, 2012, **8**, 5881-5887.
28. P. He, X. Li, M. Deng, T. Chen and H. Liang, *Soft Matter*, 2010, **6**, 1539-1546.
29. R. Toth, F. Santese, S. P. Pereira, D. R. Nieto, S. Pricl, M. Fermeglia and P. Posocco, *J. Mater. Chem.*, 2012, **22**, 5398-5409.
30. A. Alexeev, W. E. Uspal and A. C. Balazs, *ACS Nano*, 2008, **2**, 1117-1122.
31. P. Español and P. Warren, *EPL (Europhysics Letters)*, 1995, **30**, 191.
32. I. V. Neratova, A. S. Pavlov and P. G. Khalatur, *Polym. Sci. Ser. A*, 2010, **52**, 959-969.
33. R. Toth, D.-J. Voorn, J.-W. Handgraaf, J. G. E. M. Fraaije, M. Fermeglia, S. Pricl and P. Posocco, *Macromolecules*, 2009, **42**, 8260-8270.
34. A. Stenbock-Fermor, A. A. Rudov, R. A. Gumerov, L. A. Tsarkova, A. Böker, M. Möller and I. I. Potemkin, *ACS Macro Letters*, 2014, **3**, 803-807.
35. R. H. Perry and D. W. Green, *Perry's Chemical Engineer's Handbook, 7th Edition*, Mc Graw Hill, 1998.
36. R. D. Groot and P. B. Warren, *J. Chem. Phys.*, 1997, **107**, 4423-4435.
37. M. A. Horsch, Z. Zhang, C. R. Iacovella and S. C. Glotzer, *J. Chem. Phys.*, 2004, **121**, 11455-11462.
38. M. Maly, P. Posocco, S. Pricl and M. Fermeglia, *Ind. Eng. Chem. Res.*, 2008, **47**, 5023-5038.
39. P. Yang, S. Wang, X. Teng, W. Wei, V. P. Dravid and L. Huang, *J. Phys. Chem. C*, 2012, **116**, 23036-23040.
40. D. W. van Krevelen and K. t. Nijenhuis, *Properties of Polymers, 4rd Ed.*, Elsevier, 2009.
41. J. Gutierrez, A. Tercjak, I. Garcia and I. Mondragon, *Nanotechnology*, 2009, **20**, 225603.
42. S. H. Anastasiadis, T. P. Russell, S. K. Satija and C. F. Majkrzak, *Phys. Rev. Lett.*, 1989, **62**, 1852-1855.
43. T. P. Russell, G. Coulon, V. R. Deline and D. C. Miller, *Macromolecules*, 1989, **22**, 4600-4606.
44. P. F. Green, T. M. Christensen, T. P. Russell and R. Jerome, *J. Chem. Phys.*, 1990, **92**, 1478-1482.
45. P. F. Green, T. M. Christensen and T. P. Russell, *Macromolecules*, 1991, **24**, 252-255.
46. P. G. D. Gennes and J. Prost, *The Physics of Liquid Crystals*, Clarendon Press, Oxford 1993.
47. R. L. McGreevy, *Computer Modeling in Inorganic Crystallography*, Academic Press, San Diego, CA, 1997.
48. F. J. Martínez-Veracoechea and F. A. Escobedo, *Macromolecules*, 2005, **38**, 8522-8531.
49. J. Peng, X. Gao, Y. Wei, H. Wang, B. Li and Y. Han, *J. Chem. Phys.*, 2005, **122**, 114706.
50. Z. Posel, P. Posocco, M. Fermeglia, M. Lisal and S. Pricl, *Soft Matter*, 2013, **9**, 2936-2946.
51. T. K. Patra and J. K. Singh, *Soft Matter*, 2014, **10**, 1823-1830.